Scripta Materialia 258 (2025) 116527

Contents lists available at ScienceDirect

Scripta Materialia

journal homepage: www.journals.elsevier.com/scripta-materialia

Exceptional strength–ductility combination of heterostructured stainless steel for cryogenic applications

Liliana Romero-Resendiz [a,b,c], Yi Huang [b], Alexander J. Knowles [a], Joe Kelleher [d], Tung Lik Lee [d], Tayebeh Mousavi [e], Muhammad Naeem [a,*]

[a] School of Metallurgy and Materials, University of Birmingham, Birmingham B15 2TT, UK
[b] Department of Design and Engineering, Faculty of Science and Technology, Bournemouth University, Poole, Dorset BH12 5BB, UK
[c] Facultad de Química, Departamento de Ingeniería Metalúrgica, Universidad Nacional Autónoma de México, Mexico City 04510, Mexico
[d] ISIS Neutron and Muon Source, STFC Rutherford Appleton Laboratory, Harwell Campus, Didcot, Oxfordshire OX11 0QX, UK
[e] Department of Engineering, King's College London, London WC2R 2LS, UK

ARTICLE INFO

Keywords:
Heterostructured material
Mechanical properties
In-situ testing
Neutron diffraction
Cryogenic application

ABSTRACT

Heterostructured materials have been demonstrated as a new route to improve the strength–ductility trade-off of metallic materials. However, their mechanical performance at cryogenic temperatures has been scarcely explored. This study investigates the mechanical properties and phase transformation of a heterostructured and antimicrobial stainless steel (HS&AMSS), 316L+Cu, at a cryogenic temperature of 77 K. By using in-situ neutron diffraction, we revealed real-time phase evolution under tensile deformation. The HS&AMSS demonstrated exceptional mechanical properties at 77 K, including a significantly higher yield strength of 1400 MPa combined with an excellent ductility of 36 % compared to conventional stainless steels and heterostructured multicomponent alloys. The outstanding mechanical performance is attributed to the synergistic effect of multiple strengthening and strain hardening mechanisms. These findings suggest that HS&AMSS is a promising material for applications requiring robust mechanical properties in cryogenic environments, such as hydrogen storage, aerospace, superconducting magnets and polar infrastructure.

Since its initial development in 1912 [1], stainless steel has been one of the most accessible and cost-effective materials for industrial and everyday components. Due to its high strength, toughness, relatively low cost and corrosion resistance, stainless steel is used widely across society, including biomedical implants, clinical tools, refrigerators, pipelines, potable water containers, automobiles, pressure vessels, ships, architectural applications, as well as for equipment in pharmaceutical, natural resources extraction, food-processing, and petrochemical plants, among others [2–4]. However, failures or design limitations have been reported in many of these applications, due to insufficient strength/-ductility ratio during service, corrosion, and fatigue [5–10]. Therefore, improving stainless steel's mechanical properties has been of great interest to researchers and industrial communities.

Heterostructured arrangements can offer significant improvements in the trade-off between the strength and ductility of stainless steel, also using large-scalable and cost-effective fabrication routes [11]. Heterostructured materials (HSMs) are characterized and defined by their microstructure, which incorporates mutually constraining soft and hard zones to create a synergy that enhances mechanical properties [12]. This is primarily achieved through hetero-deformation induced (HDI) strengthening, distinct from those observed in homogeneous fine- or coarse-grained materials. The HDI stress arises from strain partitioning and resultant strain gradients at the soft/hard zone boundaries, necessitating geometrically necessary dislocations (GNDs) to accommodate the deformation. The stress applied to the interfaces by the GND pile-ups generates long-range back and forward stresses at the soft and hard zones, respectively, collectively producing HDI stress [12]. HDI stress contributes to the material's enhanced yield strength while retaining ductility, improving upon the conventional strength–ductility trade-off in homogeneous materials at room temperature. However, for some of the current and potential applications of stainless steel (e.g., aerospace, cryogenics, polar infrastructures, food preservation, fuel cells, etc.) adequate mechanical properties under cryogenic conditions are imperative.

In the realm of bulk heterostructured alloys, real-time microstructural studies at cryogenic temperatures remain relatively uncharted

* Corresponding author.
E-mail address: m.naeem@bham.ac.uk (M. Naeem).

https://doi.org/10.1016/j.scriptamat.2024.116527
Received 17 August 2024; Received in revised form 1 November 2024; Accepted 20 December 2024
Available online 30 December 2024

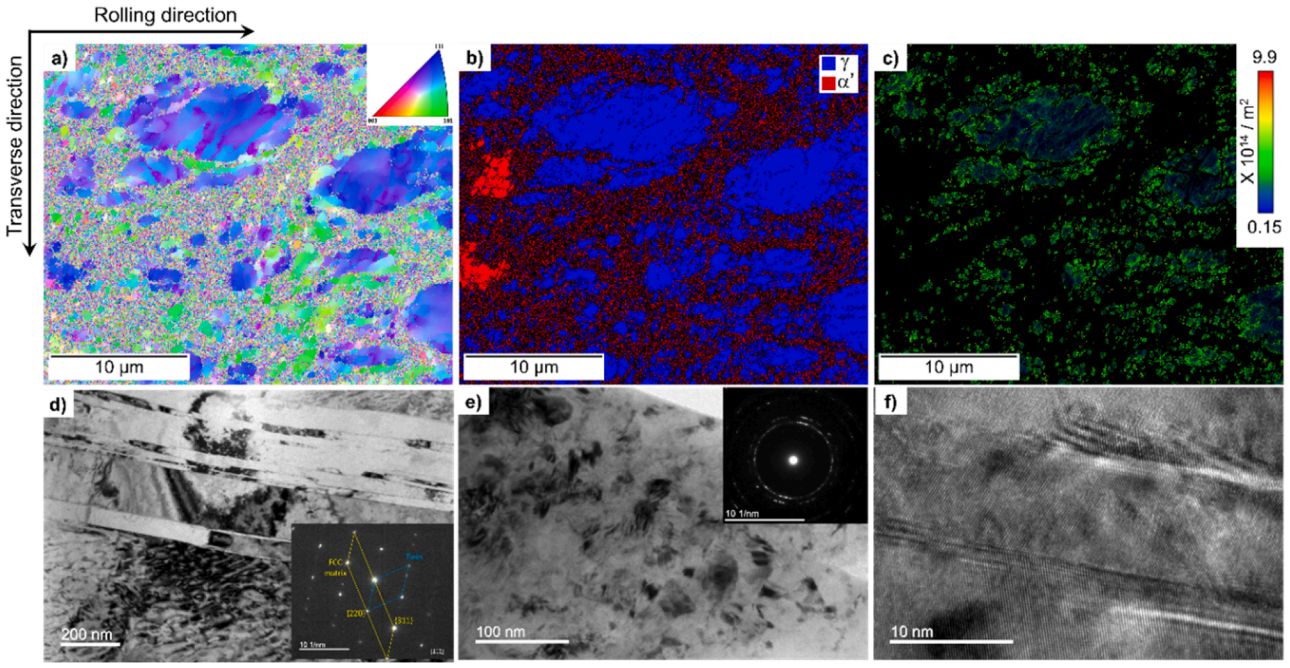

Fig. 1. Microstructural features of the HS&AMSS. a) Inverse pole figure mapping in the rolling plane, b) phase mapping, c) geometrically necessary dislocations mapping, d) nano-twins and the selected area electron diffraction (SAED) pattern as an inset, e) nano-grains and the respective SAED pattern as inset, and f) stacking faults in FCC matrix.

territory. Some post-mortem attempts to study mechanical properties of heterostructured multiphase [13,14], partially-recrystallized [15–18], and twin-gradient [19] materials at cryogenic conditions have been reported. These attempts have each shown an improved strength–ductility trade-off, attributed to the synergistic effect of multiple strengthening and strain hardening mechanisms. A strong contribution to this synergy has been repeatedly attributed to the mutual constraining between soft and hard zones and consequent generation of GND pile-ups at the soft/hard interfaces in HSMs [13–17,19]. Furthermore, the temperature-dependence of flow stress within heterostructured soft/hard zones seems to make the strain partitioning stronger, leading to improved strength–ductility trade-off [20].

In this work, real-time phase transformation evolution in a heterostructured stainless steel was studied by means of in-situ neutron diffraction at a cryogenic temperature of 77 K. Comparison is also made to reported conventional stainless steels to gain insight to the origins of the improved mechanical properties at cryogenic conditions. We used a heterostructured and antimicrobial stainless steel (HS&AMSS) comprising grain size and multiphase heterostructuring, whose antimicrobial efficacy has previously been shown [21]. This material selection not only addresses the pressing need for materials with enhanced mechanical performance but also introduces multifunctionality that could revolutionize applications under cryogenic conditions.

The raw material was 316L stainless steel cast with 3 wt.% Cu additions (316L+3Cu). 3 wt.% Cu was selected to combine antimicrobial properties below cytotoxic levels [22–24] without any discernible effect on stacking fault energy (SFE) [25,26]. Low-to-medium SFE is crucial to promote dislocation planar slip, GND pile-ups, HDI stress, twinning, and potential phase transformation [11,27]. Considering that SFE of austentitic steels increases by just ~1 mJ m^{-2} per wt.% of Cu addition [26], the reported SFE for the 316L steel of 34–44 mJ m^{-2} at room temperature [28] may increase only slightly after the addition of 3 wt.% Cu. Typically, SFE between 18 and 45 mJ m^{-2} promote twinning in austenitic steels [29,30] while phase transformation occurs for SFE <18 mJ m^{-2} [31]. The SFE typically decreases at cryogenic temperatures culminating in phase transformation [26,28,31,32], and is the focus of the current work. The HS&AMSS had chemical composition of Fe-17.38Cr-12.15Ni-2.58Mo-1.91Mn-0.02C-3.01Cu (wt.%). The optimization of the thermo-mechanical parameters has been reported elsewhere [21] and those resulting in the best combination of strength and ductility are employed for this work. A 10 mm thick plate of cast material was subjected to a solution heat treatment under Ar atmosphere at 1050 °C for 30 min, followed by aging at 650 °C for 60 min to encourage Cu precipitation. Posteriorly, cold rolling up to 80 % thickness reduction and partial recrystallization treatment at 650 °C for 60 min were employed to form the HSM. All heat treatments were performed at ~40 °C s^{-1} heating rate and finished by water quenching.

For scanning electron microscopy (SEM) and electron backscatter diffraction (EBSD), the samples were prepared to mirror-like surface finish with colloidal silica of 0.1 μm particle size and electropolished in 25 vol.% HNO_3 solution at ~77 K for 60 s with 20 V. EBSD analyses were carried out with a step size of 0.1 μm. The GND density estimation was performed from the EBSD data with AZtecCrystal software (see supplementary material Note 1). For transmission electron microscopy (TEM), the samples were ground to a thickness of 50 μm and punched into 3 mm diameter discs. Electron-transparent regions were obtained using a precision ion polishing system Gatan 695. The observations were performed in a JEOL 2100F TEM equipped with energy dispersive X-ray spectroscopy and operated at 200 kV acceleration voltage. Additionally, the automated nanodiffraction mapping of the sample deformed at 77 K was performed with ThermoFisher Talos F200X G2 TEM equipped with a DigiSTAR/ASTAR system from NanoMEGAS. A step size of 5 nm, a run of 480 × 480 pixels, a precession angle of 0.6°, a precession per frame of 2, and an acceleration voltage of 200 kV, were used during the nanodiffraction mapping acquisition.

Tensile test samples with gauge dimensions of 1.5 mm × 3.9 mm × 20 mm were used for in-situ neutron diffraction at the ENGIN-X beamline of the ISIS Pulsed Neutron and Muon Source. Uniaxial tensile testing was performed at a strain rate of 10^{-4} s^{-1} using an Instron 100 kN servohydraulic load frame equipped with a cryogenic vacuum chamber [33]. The diffraction data along both loading and transverse directions were obtained during deformation at 77 K and 293 K.

The microstructure of the undeformed HS&AMSS (316L+3Cu) is shown in Fig. 1a, comprising coarse grain colonies surrounded by nano-

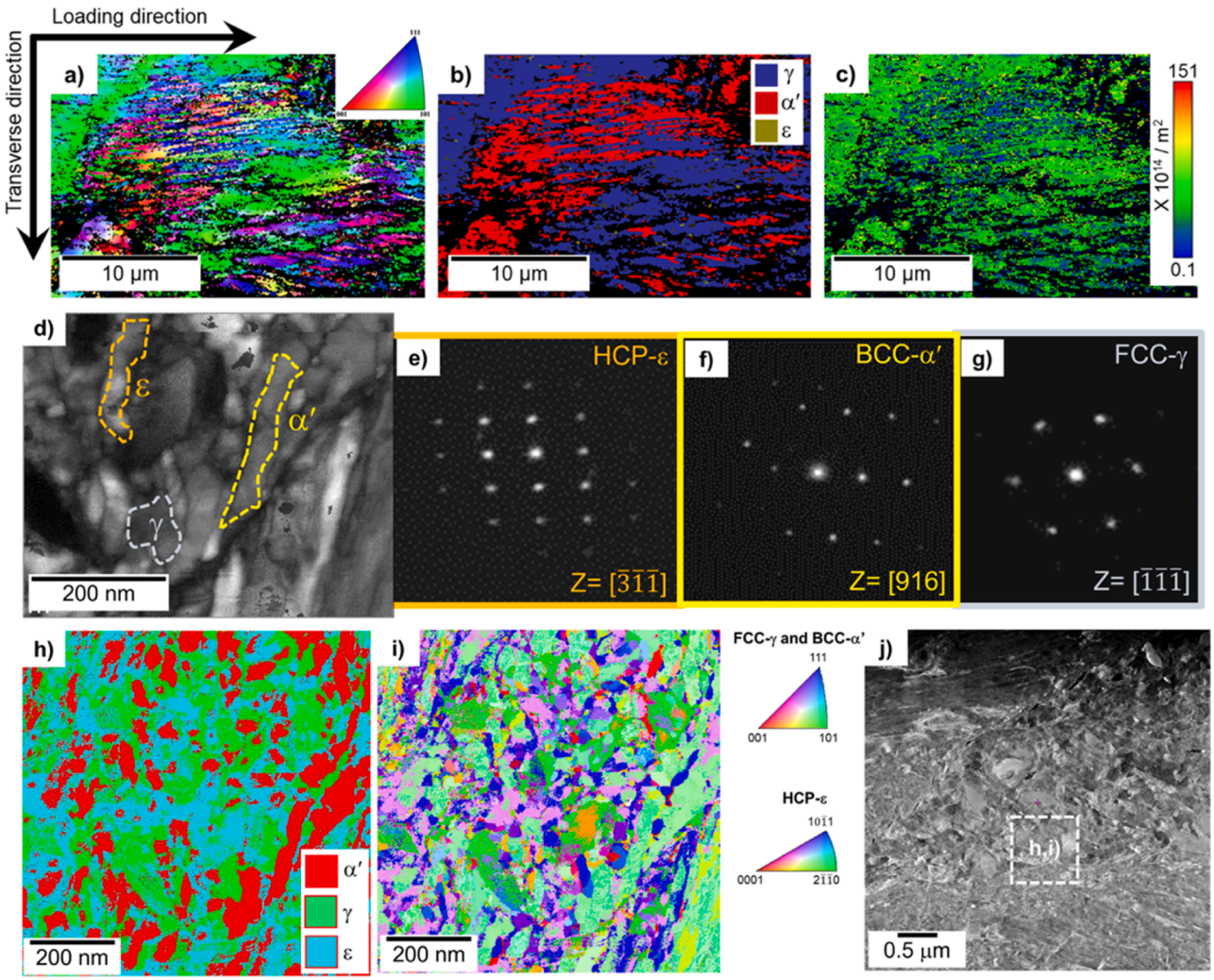

Fig. 2. Microstructural features of the HS&AMSS after deformation at 77 K. EBSD mapping along the loading direction (aligned with the rolling plane) of a) inverse pole figures, b) phases, and c) geometrically necessary dislocations. TEM nanodiffraction mapping showing the presence of ε, α', and γ phases, along with their: d) morphology, e–g) precession electron diffraction patterns, h) phases and i) orientation revealed by a TEM diffraction map obtained using NanoMEGAS in j) selected interface region between an austenite-enriched zone and α'-martensite zone (chemical mapping of this region is shown in Fig. S2).

and ultrafine-grains. The alloy contained 22.8 % of body-centered cubic (BCC) martensite (α'), 77.2 % of face-centered cubic (FCC) austenite (γ), and a GND density of 6.8 $\times$ 10^{14} m^{-2}. The α' and GNDs (Fig. 1b and c) were induced by cold rolling and persisted after partial recrystallization. Most of the GND pile-ups are located within the coarse grains (softer regions) due to their higher stress acceptance compared to the fine grains (harder regions) [12]. Fig. 1c also shows that GND pile-ups are more prominent near the coarse/fine grains interfaces. This is due to their main role in accommodating the strain gradient owing to mechanical incompatibility between the coarse and fine grains [34]. The GND pile-ups are expected to push against the coarse/fine grain interfaces with a stress proportional to the number of dislocations in the pile-up [12]. Consequently, long-range back stress is expected at the coarse-grained (softer) regions and forward stress at the fine-grained (harder) regions. The back stress pushes against the dislocation source, making it more difficult for the Frank-Read source to emit more dislocations and providing extra strengthening to the coarse-grained regions. Meanwhile, forward stress is expected to promote dislocation slip, providing extra strain hardening to the fine-grained regions. The synergy of forward and back stress, i.e., HDI stress, to improve the strength–ductility trade-off compared to conventional (homogeneous) materials has been demonstrated in many HSMs at ambient temperature [11], including in the present HS&AMSS [21]. The improved strength–ductility trade-off of the HS&AMSS is due to a combination of multiple defect-driven strengthening and strain hardening mechanisms, including nano-twins (Fig. 1d), nano-grains (Figs. 1e and S1), and stacking faults (Fig. 1f). These defects promote strain hardening through the inhibition of dynamic recovery due to cross-slip. Low-to-medium SFE also promotes more efficient grain refinement and provides nucleation sites, i.e., twins and stacking faults, for phase transformation to occur [11,27].

Following tensile deformation at 77 K, the grains become elongated in the loading direction. The microstructure consists of strip-like grains surrounded by nano- and ultrafine-grains (Fig. 2a). The deformed α' grains can be identified by their elongated irregular shapes. A 67.2 vol.% of α', 32.1 % of γ, 0.7 % of ε and GND density of 21.8 $\times$ 10^{14} m^{-2} are observed after the tensile deformation at 77 K (Fig. 2b and c). The GND pile-ups in Fig. 2c are mostly located within the softer (γ) zones and near the boundaries with α'. This is evident from the highest GND intensity within the γ zones in Fig. 2c. Thus, GNDs accommodate the strain gradient at the γ/α' interfaces. Unlike the lack of martensitic phase transformation after room temperature tensile deformation, which is consistent with the absence of phase transformation in 316L after room temperature tensile test [35], the deformation at 77 K involved strain-induced α'-martensite thus leading to the transformation-induced plasticity (TRIP) effect. Cryogenic temperature increases the driving

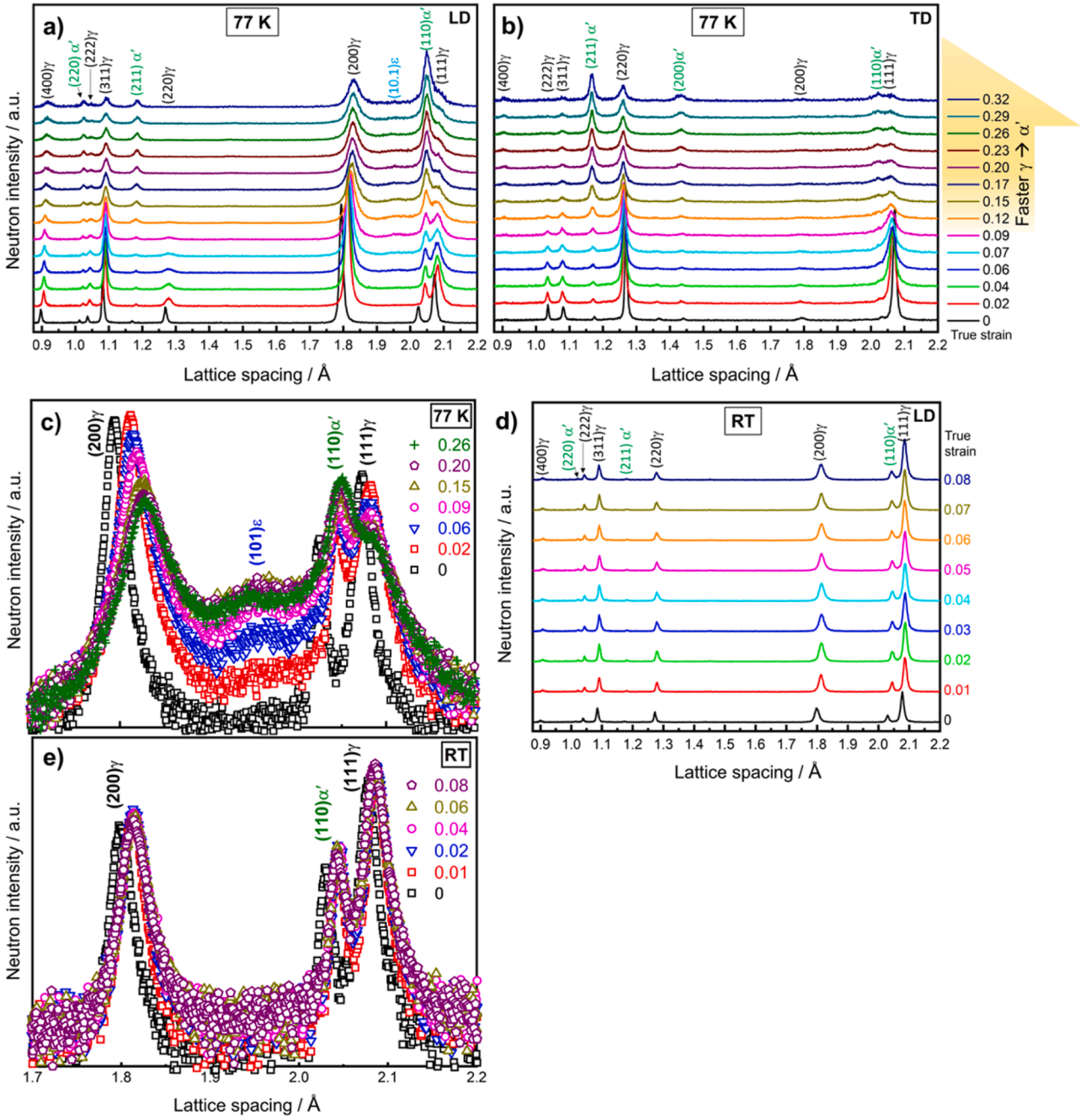

Fig. 3. Phase evolution of HS&AMSS during in-situ tensile testing using neutron diffraction. Diffraction patterns during deformation at 77 K along the a) loading direction (LD) and b) transversal direction (TD). d) Phase evolution during deformation at room temperature along LD. The selected patterns along LD showing zoomed-in region, d-spacing range from 1.7 to 2.2 Å and the intensity plotted in logarithmic scale, highlighting: c) the formation of HCP (10.1) peak and the development of α'-martensite at the expense of γ phase at 77 K, and e) the lack of HCP phase and the nearly constant α'-martensite and γ contents during deformation at room temperature.

force for strain-induced γ-to-α' transformation [36,37]. This occurs because α' nucleation sites, such as stacking faults and twins, are formed from partial dislocation gliding, which is encouraged at low temperatures [31,38].

To comprehensively identify nanoscale phases present in the cryogenically deformed HS&AMSS, we used nanobeam precession diffraction mapping with NanoMEGAS. The selected analysis zone was at the austenite/martensite interface (Fig. S2), where the austenite phase was characterized by higher levels of γ-stabilizers, i.e., Cr, Ni, and Mo (Fig. S2). Fig. 2d,e,h, reveals the formation of hexagonal close-packed (HCP) ε-martensite during cryogenic deformation. The volume fraction of ε phase in Fig. 2h appears comparable to other phases. However, it should be noted that the distribution of phases at the α'/γ interface (~0.5 μm^2, Fig. 2h) may not represent the bulk material, as larger EBSD scans (~500 μm^2, Fig. 2b) indicated only traces of ε phase. Neutron diffraction, covering ~20 mm^2 area across the entire sample thickness, was employed to examine the bulk phase evolution (Fig. 3). The diffraction patterns in Fig. 2f and g also confirm α' and γ phases. Phase mapping in Fig. 2h reveals that ε, α', and γ phases are distributed relatively uniformly within the examined zone. Nano-sized features of these phases, produced during cryogenic deformation, can be further analysed by the orientation mapping in Fig. 2i. The interfaces in Fig. 2h

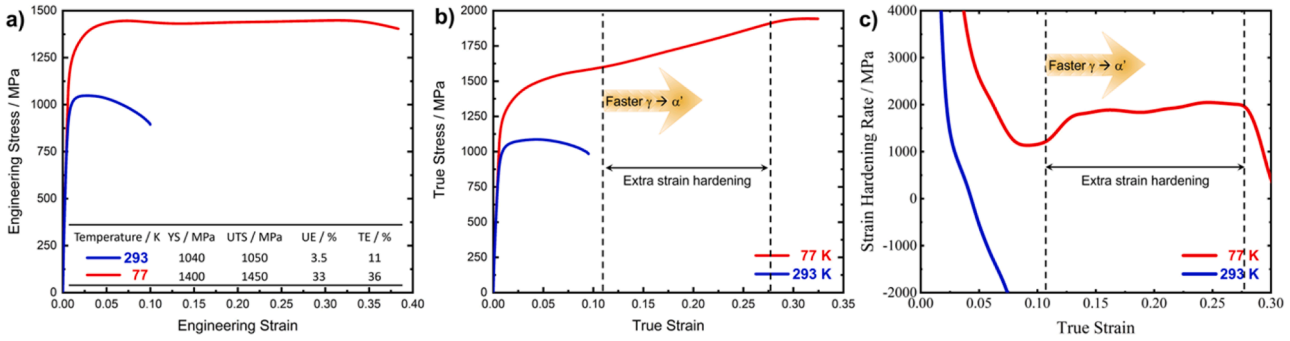

Fig. 4. Mechanical behavior of HS&AMSS at 77 and 293 K. a) Engineering stress-strain curves, b) true stress-strain curves, and c) strain hardening rate curves. The yield strength (YS), ultimate tensile strength (UTS), uniform elongation (UE), and total elongation (TE) are listed inside a).

indicate interconnectedness due to the progressive transformation pathway of $\gamma \rightarrow \varepsilon \rightarrow \alpha'$. The formation of the ε phase in austenitic stainless steel is widely recognized as an intermediate step in the $\gamma \rightarrow \varepsilon \rightarrow \alpha'$ transformation pathway, which is particularly promoted at cryogenic temperatures [35–38].

The phase evolution during in-situ tensile deformation with neutron diffraction is presented in Fig. 3. At 77 K, the γ-to-α' phase transformation is evident from an early deformation strain and becomes massive from a tensile strain of ~0.12, where the (110)-α', (211)-α', and (220)-α' peaks become more evident, while the peaks associated with the γ-phase significantly decrease in intensity (Fig. 3a and b). The effect of cryogenic temperature in lowering SFE and encouraging the $\gamma \rightarrow \alpha'$ and $\gamma \rightarrow \varepsilon \rightarrow \alpha'$ transformation (Fig. 3a–c) can be demonstrated by the comparative phase evolution during deformation at room temperature in Fig. 3d. Fig. 3c highlights the formation of ε-martensite during deformation at 77 K. The ε phase grows from the HCP-stacking sequence formed by partial dislocations gliding [35,39]. The formation of ε is favored for low SFE materials [38], where lower temperatures decrease the SFE [31,32,40]. It is a metastable phase that occurs during the strain-induced phase transformation of $\gamma \rightarrow \varepsilon \rightarrow \alpha'$ [35,36,38]. The metastable nature of the ε phase can be observed by the characteristic (10.1)-ε peak appearing at a strain of ~0.06 which becomes weak towards the end of the deformation due to $\varepsilon \rightarrow \alpha'$ transformation. Other studies have reported a significant strain hardening contribution during the $\gamma \rightarrow \varepsilon \rightarrow \alpha'$ transformation at cryogenic temperatures [35,41,42]. This is related to the formation of massive α' nucleation sites under conditions that promote low SFE, such as low temperature. Intersections of ε plates, with active slip systems, or with twin boundaries, provide nucleation sites for strain-induced embryos of α' [38]. Due to the above, α' has been favorably found near stacking faults or ε phase [35]. The effect of lower SFE at cryogenic temperature is further evidenced by the absence of any phase transformation during deformation of HS&AMSS at room temperature (Fig. 3c vs. e).

The overall mechanical performance of the HS&AMSS increased enormously at 77 K compared to 293 K (Fig. 4). The yield strength (YS), ultimate tensile strength (UTS), uniform elongation (UE), and total elongation (TE) increased by 35 %, 38 %, 842 %, and 227 %, respectively, at 77 K compared to 293 K (Fig. 4a). The true stress-strain curves (Fig. 4b) show continuously increasing stress during deformation at 77 K, while the sample at 293 K showed a decreasing tendency from a strain of ~0.04. The large difference between UTS and YS in Fig. 4b at 77 K suggests higher work hardening capability, which is demonstrated by the strain hardening rate in Fig. 4c. The rise of strain hardening rate from strain of ~0.11 at 77 K agrees with the faster $\gamma \rightarrow \alpha'$ phase transformation, as well as occurrence of $\gamma \rightarrow \varepsilon$ shown in Figs. 2 and 3.

Therefore, phase transformation, i.e., TRIP effect, is the main contributor to the extra strain hardening observed from ~0.11 to ~0.28 at 77 K. The decline of the work hardening rate after ~0.28 strain may be related to the exhaustion of phase transformation, which agrees with the reported plasticity mechanisms of 316L stainless steel at cryogenic temperature [35]. On the other hand, the strain hardening rate of the sample tested at 293 K dropped below zero soon after the plastic deformation began. Given the extra strain hardening, the HS&AMSS at 77 K accommodates a larger true strain up to ~0.33 compared to that of ~0.09 at 293 K.

Fig. 5 demonstrates the mechanical properties comparison of the HS&AMSS from this study with the literature. Yield strength data for traditional homogeneous stainless steels (Fig. 5a) with temperature has significantly lower yield strength compared to the HS&AMSS across the whole temperature range. Fig. 5b presents the strength–ductility trade-off at 77 K, comparing heterostructured high- and medium-entropy multicomponent alloys with HS&AMSS. The HS&AMSS demonstrates a superior combination of yield strength and uniform elongation, outperforming multicomponent heterostructured alloys. Based on our

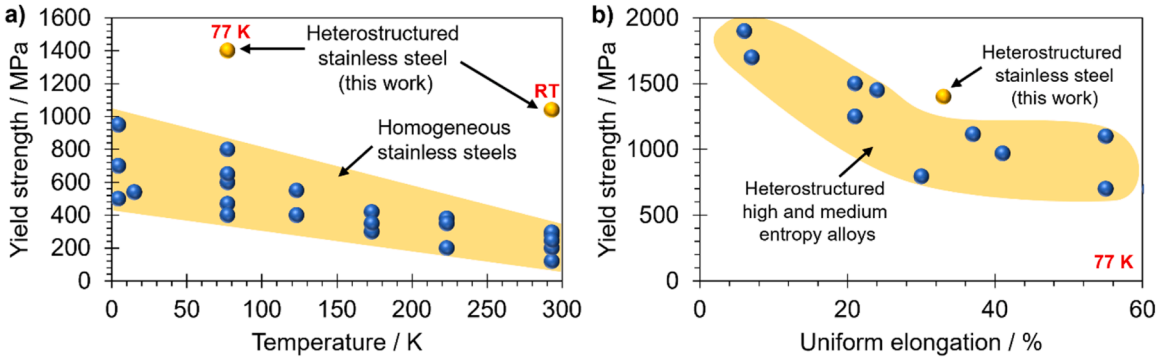

Fig. 5. Comparison of mechanical properties among the HS&AMSS of this work (heterostructured stainless steel) and other reported materials. a) Dependence of yield strength with the temperature of conventional (homogeneous) stainless steels [28,35,43–45] and the HS&AMSS, and b) strength–ductility trade-off of heterostructured multicomponent materials studied at 77 K [13–19] and comparison with the current HS&AMSS.

abovementioned results, the effect of the heterostructured arrangement may be further stimulated by the ε-phase mainly found near the γ/α' interfaces (Fig. 2), the efficient formation of hard α' (Fig. 3), and increment of defects like dislocations (Fig. 2) during deformation at 77 K. The synergistic effect between the dislocation-blocking capability of defects (translated into strengthening) and the formation of new phase or domain regions with available sites for dislocation accumulation (translated into ductility) drives the improved strength–ductility of the HS&AMSS.

In conclusion, the mechanical behavior and phase transformation of HS&AMSS were investigated in-situ at cryogenic (77 K) and room (293 K) temperatures. The HS&AMSS exhibited significantly higher yield strength of 1400 MPa and almost four times higher ductility at 77 K compared to 293 K, highlighting its superior performance in cryogenic environments. The enhanced mechanical properties at 77 K primarily stemmed from the strain partitioning-driven GND pile-ups at the boundaries of soft and hard zones, and the $\gamma \rightarrow \alpha'$ and $\gamma \rightarrow \varepsilon \rightarrow \alpha'$ phase transformations. Together, transformation-induced plasticity and GND pile-ups contributed to the extra strain hardening and strengthening observed at cryogenic temperature. Comparison with reported conventional stainless steels and heterostructured multicomponent alloys indicated that the HS&AMSS has a superior combination of yield strength and uniform elongation, making it highly suitable for cryogenic applications in hydrogen storage, aerospace, nuclear, and marine engineering.

CRediT authorship contribution statement

Liliana Romero-Resendiz: Writing – review & editing, Writing – original draft, Methodology, Investigation, Formal analysis, Conceptualization, Project administration. **Yi Huang:** Writing – review & editing, Validation. **Alexander J. Knowles:** Writing – review & editing, Validation. **Joe Kelleher:** Writing – review & editing, Methodology. **Tung Lik Lee:** Writing – review & editing, Methodology. **Tayebeh Mousavi:** Formal analysis, Methodology, Writing – review & editing. **Muhammad Naeem:** Writing – review & editing, Writing – original draft, Project administration, Methodology, Investigation, Formal analysis, Conceptualization.

Declaration of competing interest

The authors declare that they have no known competing financial interests or personal relationships that could have appeared to influence the work reported in this paper.

Acknowledgments

This work was supported by the HORIZON EUROPE programme of research and innovation of the European Union under the Marie Sklodowska-Curie Actions and financed by the UK Research and Innovation, (EP/Y020545/1) and Programa de Apoyo a Proyectos de Investigación e Innovación Tecnológica (PAPIIT-IA102724). A.J.K. acknowledges support from the Royal Academy of Engineering Research Fellowship (RF\201819\18\158) and UKRI Future Leaders Fellowship (MR/ T019174/1). The authors gratefully acknowledge the UK's Science and Technology Facilities Council (STFC) for access to neutron beamtime (RB2220253) at ENGIN-X, ISIS Neutron and Muon Source, Rutherford Appleton Laboratory.

Supplementary materials

Supplementary material associated with this article can be found, in the online version, at doi:10.1016/j.scriptamat.2024.116527.

References

[1] J.D. Verhoeven, Metallurgy of steel for bladesmiths & others who heat treat and forge steel, 2005.
[2] L. Gardner, Stability and design of stainless steel structures—Review and outlook, Thin-Walled Struct. 141 (2019) 208–216, https://doi.org/10.1016/j.tws.2019.04.019.
[3] A. Hemmasian Ettefagh, S. Guo, J. Raush, Corrosion performance of additively manufactured stainless steel parts: a review, Addit. Manuf. 37 (2021) 101689, https://doi.org/10.1016/j.addma.2020.101689.
[4] R.T. Loto, Electrochemical corrosion characteristics of 439 ferritic, 301 austenitic, S32101 duplex and 420 martensitic stainless steel in sulfuric acid/NaCl solution, J. Bio Tribocorros. 3 (2017) 1–8, https://doi.org/10.1007/s40735-017-0084-1.
[5] J. You, S. Kim, J. Oh, H. Choi, M. Jih, Removal of a fractured needle during inferior alveolar nerve block: two case reports, J. Dent. Anesth. Pain Med. 17 (2017) 225–229, https://doi.org/10.17245/jdapm.2017.17.3.225.
[6] K. Ravindranath, R. Alazemi, Failure of stainless steel 304L air cooler tubes due to stress corrosion cracking caused by organic chlorides, Eng. Fail. Anal. 102 (2019) 79–86, https://doi.org/10.1016/j.engfailanal.2019.04.029.
[7] G. Manivasagam, D. Dhinasekaran, A. Rajamanickam, Biomedical implants: corrosion and its prevention—A review, Recent Pat. Corros. Sci. 2 (2010) 40–54, https://doi.org/10.2174/1877610801002010040.
[8] V.M. Linton, N.J. Laycock, S.J. Thomsen, A. Klumpers, Failure of a super duplex stainless steel reaction vessel, Eng. Fail. Anal. 11 (2004) 243–256, https://doi.org/10.1016/j.engfailanal.2003.05.011.
[9] M.S. Kumar, M. Sujata, M.A. Venkataswamy, S.K. Bhaumik, Failure analysis of a stainless steel pipeline, Eng. Fail. Anal. 15 (2008) 497–504, https://doi.org/10.1016/j.engfailanal.2007.05.002.
[10] R.W. Fuller, J.Q. Ehrgott, W.F. Heard, S.D. Robert, R.D. Stinson, K. Solanki, M. F. Horstemeyer, Failure analysis of AISI 304 stainless steel shaft, Eng. Fail. Anal. 15 (2008) 835–846, https://doi.org/10.1016/j.engfailanal.2007.11.001.
[11] L. Romero-Resendiz, M. El-Tahawy, T. Zhang, M.C. Rossi, D.M. Marulanda-Cardona, T. Yang, V. Amigó-Borrás, Y. Huang, H. Mirzadeh, I.J. Beyerlein, J. C. Huang, T.G. Langdon, Y.T. Zhu, Heterostructured stainless steel: properties, current trends, and future perspectives, Mater. Sci. Eng. R 150 (2022) 100691, https://doi.org/10.1016/j.mser.2022.100691.
[12] Y. Zhu, X. Wu, Heterostructured materials, Prog. Mater. Sci. 131 (2023) 101019, https://doi.org/10.1016/j.pmatsci.2022.101019.
[13] J.M. Park, J. Moon, J.W. Bae, D.H. Kim, Y.H. Jo, S. Lee, H.S. Kim, Role of BCC phase on tensile behavior of dual-phase $Al_{0.5}$CoCrFeMnNi high-entropy alloy at cryogenic temperature, Mater. Sci. Eng. A 746 (2019) 443–447, https://doi.org/10.1016/j.msea.2019.01.041.
[14] D.D. Zhang, J.Y. Zhang, J. Kuang, G. Liu, J. Sun, The B2 phase-driven microstructural heterogeneities and twinning enable ultrahigh cryogenic strength and large ductility in NiCoCr-based medium-entropy alloy, Acta Mater. 233 (2022) 117981, https://doi.org/10.1016/j.actamat.2022.117981.
[15] H. Peng, L. Hu, L. Li, H. Wang, Y. Zhang, S. Huang, L. Li, I. Baker, Excellent cryogenic mechanical properties of a novel medium-entropy alloy via vanadium-doping and hetero-grain/precipitation engineering, Mater. Charact. 207 (2024) 113600, https://doi.org/10.1016/j.matchar.2023.113600.
[16] P. Sathiyamoorthi, P. Asghari-Rad, J.M. Park, J. Moon, J.W. Bae, A. Zargaran, H. S. Kim, Exceptional cryogenic strength-ductility synergy in $Al_{0.3}$CoCrNi medium-entropy alloy through heterogeneous grain structure and nano-scale precipitates, Mater. Sci. Eng. A 766 (2019) 138372, https://doi.org/10.1016/j.msea.2019.138372.
[17] J.W. Bae, J. Lee, A. Zargaran, H.S. Kim, Enhanced cryogenic tensile properties with multi-stage strain hardening through partial recrystallization in a ferrous medium-entropy alloy, Scr. Mater. 194 (2021) 113653, https://doi.org/10.1016/j.scriptamat.2020.113653.
[18] Y.H. Jo, S. Jung, W.M. Choi, S.S. Sohn, H.S. Kim, B.J. Lee, N.J. Kim, S. Lee, Cryogenic strength improvement by utilizing room-temperature deformation twinning in a partially recrystallized VCrMnFeCoNi high-entropy alloy, Nat. Commun. 8 (2017) 1–8, https://doi.org/10.1038/ncomms15719.
[19] Z. An, S. Mao, C. Jiang, Z. Li, S. Wu, Y. Zhai, L. Wang, Y. Liu, Z. Zhang, X. Han, Achieving superior combined cryogenic strength and ductility in a high-entropy alloy via the synergy of low stacking fault energy and multiscale heterostructure, Scr. Mater. 239 (2024) 115809, https://doi.org/10.1016/j.scriptamat.2023.115809.
[20] W. Su, M. Wang, F. Guo, H. Ran, Q. Cheng, Q. Wang, Y. Zhu, X. Ma, C. Huang, Heterostructure enables anomalous improvement of cryogenic mechanical properties in titanium, Acta Mater. 273 (2024) 119982, https://doi.org/10.1016/j.actamat.2024.119982.
[21] L. Romero-Resendiz, H.J. Kong, T. Zhang, H. Ni, S. Chen, M. Naeem, Y.T. Zhu, Achieving antimicrobial and superior mechanical properties in a scalable and cost-effective heterostructured stainless steel, Mater. Sci. Eng. A 886 (2023) 145676, https://doi.org/10.1016/j.msea.2023.145676.
[22] Y. Dong, J. Li, D. Xu, G. Song, D. Liu, H. Wang, M. Saleem Khan, K. Yang, F. Wang, Investigation of microbial corrosion inhibition of Cu-bearing 316L stainless steel in the presence of acid producing bacterium *Acidithiobacillus caldus* SM-1, J. Mater. Sci. Technol. 64 (2021) 176–186, https://doi.org/10.1016/j.jmst.2020.05.070.
[23] I.T. Hong, C.H. Koo, Antibacterial properties, corrosion resistance and mechanical properties of Cu-modified SUS 304 stainless steel, Mater. Sci. Eng. A 393 (2005) 213–222, https://doi.org/10.1016/j.msea.2004.10.032.
[24] D. Sun, D. Xu, C. Yang, M.B. Shahzad, Z. Sun, J. Xia, J. Zhao, T. Gu, K. Yang, G. Wang, An investigation of the antibacterial ability and cytotoxicity of a novel

cu-bearing 317L stainless steel, Sci. Rep. 6 (2016) 1–13, https://doi.org/10.1038/srep29244.
[25] A. Dumay, J.P. Chateau, S. Allain, S. Migot, O. Bouaziz, Influence of addition elements on the stacking-fault energy and mechanical properties of an austenitic Fe-Mn-C steel, Mater. Sci. Eng. A 483–484 (2008) 184–187, https://doi.org/10.1016/j.msea.2006.12.170.
[26] Y.-K. Lee, S.-J. Lee, J. Han, Critical assessment 19: stacking fault energies of austenitic steels, Mater. Sci. Technol. 32 (2016) 1–8, https://doi.org/10.1080/02670836.2015.1114252.
[27] P.-L. Sun, Y.H. Zhao, J.C. Cooley, M.E. Kassner, Z. Horita, T.G. Langdon, E. J. Lavernia, Y.T. Zhu, Effect of stacking fault energy on strength and ductility of nanostructured alloys: an evaluation with minimum solution hardening, Mater. Sci. Eng. A 525 (2009) 83–86, https://doi.org/10.1016/j.msea.2009.06.030.
[28] M.R. Crivoi, J.J. Hoyos, M.T. Izumi, D.J.M. de Aguiar, R.S. Namur, A.L. Terasawa, O.M. Cintho, In situ analysis of cryogenic strain of AISI 316L stainless steel using synchrotron radiation, Cryogenics 105 (2020) 103020, https://doi.org/10.1016/j.cryogenics.2019.103020.
[29] S. Allain, J.P. Chateau, O. Bouaziz, S. Migot, N. Guelton, Correlations between the calculated stacking fault energy and the plasticity mechanisms in Fe-Mn-C alloys, Mater. Sci. Eng. A 387–389 (2004) 158–162, https://doi.org/10.1016/j.msea.2004.01.059.
[30] B.C. De Cooman, Y. Estrin, S.K. Kim, Twinning-induced plasticity (TWIP) steels, Acta Mater. 142 (2018) 283–362, https://doi.org/10.1016/j.actamat.2017.06.046.
[31] S. Curtze, V.-T.T. Kuokkala, Dependence of tensile deformation behavior of TWIP steels on stacking fault energy, temperature and strain rate, Acta Mater. 58 (2010) 5129–5141, https://doi.org/10.1016/j.actamat.2010.05.049.
[32] L. Rémy, A. Pineau, B. Thomas, Temperature dependence of stacking fault energy in close-packed metals and alloys, Mater. Sci. Eng. 36 (1978) 47–63, https://doi.org/10.1016/0025-5416(78)90194-5.
[33] O. Kirichek, J.D. Timms, J.F. Kelleher, R.B.E. Down, C.D. Offer, S. Kabra, S. Y. Zhang, Sample environment for neutron scattering measurements of internal stresses in engineering materials in the temperature range of 6 K to 300 K, Rev. Sci. Instrum. 88 (2017) 025103, https://doi.org/10.1063/1.4974815.
[34] M.F. Ashby, The deformation of plastically non-homogeneous materials, Philos. Mag. 21 (1970) 399–424, https://doi.org/10.1080/14786437008238426.
[35] Y. Ma, M. Naeem, L. Zhu, H. He, X. Sun, Z. Yang, F. He, S. Harjo, T. Kawasaki, X.-L. Wang, Microscopic insights of the extraordinary work-hardening due to phase transformation, Acta Mater. 270 (2024) 119822, https://doi.org/10.1016/j.actamat.2024.119822.
[36] J.A. Venables, The martensite transformation in stainless steel, Philos. Mag. 7 (1962) 35–44, https://doi.org/10.1080/14786436208201856.
[37] R.P. Reed, The spontaneous martensitic transformations in 18 % Cr, 8 % Ni steels, Acta Metall. 10 (1962) 865–877, https://doi.org/10.1016/0001-6160(62)90101-3.
[38] G.B. Olson, M. Cohen, A mechanism for the strain-induced nucleation of martensitic transformations, J. Less-Common Metals 28 (1972) 107–118, https://doi.org/10.1016/0022-5088(72)90173-7.
[39] M. Naeem, H. Zhou, H. He, S. Harjo, T. Kawasaki, S. Lan, Z. Wu, Y. Zhu, X.-L. Wang, Martensitic transformation in CrCoNi medium-entropy alloy at cryogenic temperature, Appl. Phys. Lett. 119 (2021) 131901, https://doi.org/10.1063/5.0067268.
[40] K.V. Werner, M. Naeem, F. Niessen, L. Zhu, M. Villa, X.-L. Wang, M.A.J. Somers, Experimental and computational assessment of the temperature dependency of the stacking fault energy in face-centered cubic high-entropy alloys, Acta Mater. 278 (2024) 120271, https://doi.org/10.1016/j.actamat.2024.120271.
[41] S. Chen, H.S. Oh, B. Gludovatz, S.J. Kim, E.S. Park, Z. Zhang, R.O. Ritchie, Q. Yu, Real-time observations of TRIP-induced ultrahigh strain hardening in a dual-phase CrMnFeCoNi high-entropy alloy, Nat. Commun. 11 (2020) 826, https://doi.org/10.1038/s41467-020-14641-1.
[42] N. Tsuchida, E. Ishimaru, M. Kawa, Role of deformation-induced martensite in TRIP effect of metastable austenitic steels, ISIJ Int. 61 (2021) 556–563, https://doi.org/10.2355/ISIJINTERNATIONAL.ISIJINT-2020-253.
[43] T.S. Byun, N. Hashimoto, K. Farrell, Temperature dependence of strain hardening and plastic instability behaviors in austenitic stainless steels, Acta Mater. 52 (2004) 3889–3899, https://doi.org/10.1016/j.actamat.2004.05.003.
[44] W. Han, Y. Liu, F. Wan, P. Liu, X. Yi, Q. Zhan, D. Morrall, S. Ohnuki, Deformation behavior of austenitic stainless steel at deep cryogenic temperatures, J. Nucl. Mater. 504 (2018) 29–32, https://doi.org/10.1016/j.jnucmat.2018.03.019.
[45] K. Shibata, T. Ogata, A. Nyilas, T. Yuri, H. Fujii, S. Ohmiya, T. Onishi, K.P. Weiss, Comparison of strength and serration at cryogenic temperatures among 304L, 316L and 310S steels, AIP Conf. Proc. 986 (2008) 108–115, https://doi.org/10.1063/1.2900332.